Grain Boundary Sliding and Amorphization are Responsible for the Reverse Hall-Petch Relation in Superhard Nanocrystalline Boron Carbide

Dezhou Guo,[1,*] Shuangxi Song,[2,*] Ruichun Luo,[2] William A. Goddard III,[3] Mingwei Chen,[2,4] Kolan Madhav Reddy,[2,†] and Qi An[1,5,†]

[1]*Department of Chemical and Materials Engineering, University of Nevada, Reno, Nevada 89557, USA*
[2]*State Key Laboratory of Metal Matrix Composites, School of Materials Science and Engineering, Shanghai Jiao Tong University, Shanghai 200240, China*
[3]*Materials and Process Simulation Center, California Institute of Technology, Pasadena, California 91125, USA*
[4]*Department of Materials Science and Engineering, Johns Hopkins University, Baltimore, Maryland 21218, USA*
[5]*Nevada Institute for Sustainability, University of Nevada, Reno, Nevada, 89557, USA*

(Received 4 June 2018; published 4 October 2018)

The recent observation of the reverse Hall-Petch relation in nanocrystalline ceramics offers a possible pathway to achieve enhanced ductility for traditional brittle ceramics via the nanosize effect, just as nanocrystalline metals and alloys. However, the underlying deformation mechanisms of nanocrystalline ceramics have not been well established. Here we combine reactive molecular dynamics (RMD) simulations and experimental transmission electron microscopy to determine the atomic level deformation mechanisms of nanocrystalline boron carbide (B_4C). We performed large-scale (up to ~3 700 000 atoms) ReaxFF RMD simulations on finite shear deformation of three models of grain boundaries with grain sizes from 4.84 (135 050 atoms) to 14.64 nm (3 702 861 atoms). We found a reverse Hall-Petch relationship in nanocrystalline B_4C in which the deformation mechanism is dominated by the grain boundary (GB) sliding. This GB sliding leads to the amorphous band formation at predistorted icosahedral GB regions with initiation of cavitation within the amorphous bands. Our simulation results are validated by the experimental observations of an intergranular amorphous GB phase due to GBs sliding under indentation experiments. These theoretical and experimental results provide an atomistic explanation for the influence of GBs on the deformation behavior of nanocrystalline ceramics, explaining the reverse Hall-Petch relation.

DOI: 10.1103/PhysRevLett.121.145504

In polycrystalline metals, grain boundaries (GBs) act as obstacles for mobile dislocations [1,2], so that decreasing grain size increases the maximum yield strength up to the point at which GBs start to slide, which is known as the well-established Hall-Petch relationship. Application of this Hall-Petch relationship to nanocrystalline ceramics would be especially attractive because it might be expected to achieve both high strength and enhanced ductility similar to that of metals [3]. However, although conventional Hall-Petch relationship has been observed in nanocrystalline ceramics [4], its mechanisms remain unknown because the dislocation migration so important in metals is usually absent in most ceramics. In addition, the Hall-Petch relationship breaks down in metal alloys when grain size is reduced below a critical value, where the strength and hardness decrease with grain sizes [5–7]. This is because the activation of dislocations requires a higher stress than that of other deformation mechanisms such as GB sliding, GB diffusion, and GB rotation [8,9]. Indeed, recent experiments on nanocrystalline magnesium aluminate ($MgAl_2O_4$) spinel showed the Hall-Petch relationship breaks down as the grain size decreases to ~20 nm [10]. This suggests that GBs play a quite different role in the deformation and failure mechanisms of ceramics as compared to metals although the grain size effects might be similar in metals and ceramics.

Mechanical responses of nanocrystalline ceramics have been examined by means of both experiment and computer simulations [10–15]. However, the results on nanocrystalline ceramics are scarce and the breakdown of the Hall-Petch relationship remains controversial. For example, Ryou *et al.* [10] showed in $MgAl_2O_4$ ceramic that the maximum hardness at a grain of 18.4 nm and a reverse Hall-Petch region were observed as the grain size is decreased to 5 nm. They found the presence of nanocracks near triple junctions with increasing grain boundary volume fraction as the grain size reduced from 18.4 to below 5 nm. Liao *et al.* [11] showed a 50 GPa hardness of nanocrystalline SiC when the grain sizes are 10 to 20 nm and the crystalline fractions are in the range of 80%–85%. Later, Szlufaraka *et al.* [12] revealed the crossovers from intergranular continuous deformation to intragrain discrete deformation arising from the interplay between cooperative grain sliding, grain rotations, and intergranular dislocation formation. Although these molecular dynamics (MD) results indicate an essential role of switching from deformation dominated by crystallization to deformation

dominated by disordering, the dynamics in the GB phase transition and the physical mechanisms of the local amorphization are not well understood.

Superhard ceramics provide the possibility of local amorphization at GBs under deformation, which is not expected in metal alloys. However, the complex structures and chemical bonding in GBs [13,14] obscure the dynamics in the GB phase transition and the physical mechanisms of the local amorphization since it is hard to characterize the atomistic structures within such highly inhomogeneous microstructures experimentally [15]. As a model system for examining how GBs affect the mechanical response of superhard ceramics, we selected boron carbide (B_4C) because of its superior properties such as high hardness, high Hugoniot elastic limit (HEL), low density [16–21], and its abnormal shear strength reduction under high pressures [22–24]. Previous experiments revealed that amorphous shear band formation is the dominant deformation and failure mode of B_4C resulting in shear softening and brittle failure [25–27]. We have recently explained the origin of the amorphous shear band formation and its role in brittle failure [28,29].

In this Letter, we examine the deformation mechanism of nanocrystalline B_4C (n-B_4C) by combining state-of-the-art spherical-aberration (Cs)-corrected atomic resolution transmission electron microscopy (TEM) experiments with reactive molecular dynamics (RMD) simulations using the ReaxFF reactive force field. We performed RMD simulations on finite shear deformations of three models of n-B_4C at room temperature. Indeed, our RMD simulations find the reverse Hall-Petch relationship in n-B_4C with the main deformation mechanism being GBs sliding. We employed annular bright field STEM (ABF-STEM) to give clear evidence of the amorphous GB phase formed by GB sliding under nanoindentation at ambient temperature that causes the relative plastic deformation in n-B_4C. The experimentally observed GB deformation and amorphization provide direct evidence of GBs sliding that validate our RMD simulations in n-B_4C.

Deformation mechanism of nanocrystalline B_4C *from RMD simulations*.—In order to illustrate the deformation mechanism of n-B_4C, we constructed three n-B_4C models using a Voronoi polyhedral approach [the details are described in the Supplemental Material [30]]. The grain size varies from 4.84 to 14.64 nm to illustrate the grain size effects on the strength of n-B_4C, as shown in Fig. S1 of the Supplemental Material [30].

Figure 1(a) displays the shear-stress−shear-strain relationships of these three n-B_4C models under finite shear deformation. The maximum shear stresses for these three n-B_4C models are 28.45 GPa for GB1, 29.07 GPa for GB2, and 29.25 GPa for GB3. The shear-strength−grain-size relationship is plotted in Fig. 1(b) showing that the shear strength increases as the grain size increases to ∼15 nm. This is the same reverse Hall-Petch relationship observed in $MgAl_2O_4$ [10] and metal alloys [34].

To explain this reverse Hall-Petch relationship in n-B_4C and extract the detailed deformation mechanism, we show snapshots of the three n-B_4C systems at critical shear strains in Figs. 1(c1)–1(e3). To examine the local atomic shear, we computed the von Mises shear strain n_i^{Mises} for each atom [35] (the details are shown in the Supplemental Material [30]):

The detailed deformation process involves the following steps:

(i) The shear stress τ decreases continuously at a constant rate from the initial structure indicating holistic elastic deformation. The linear elasticity ends at the shear strain of 0.25, 0.275, and 0.3 for GB1, GB2, and GB3 systems, respectively. During this process, no significant local deformation is observed, as shown in Figs. 1(c1), 1(d1), and 1(e1).

(ii) For larger strains we observe a decreased slope in the shear-stress−shear-strain curves suggesting a plastic deformation process. For the GB1 model with the smallest grain size, we observed a relatively large plastic deformation range, from 0.25 to 0.5 shear strain, representing being more ductile than the other two GB models that possess larger grain sizes. For the GB2 and GB3 models, only a narrow plastic deformation range (∼0.05 shear strain) is observed, indicating a brittle character for larger grain n-B_4C. The von Mises shear strain analysis indicates that the most slipped atoms distribute within the GB regions for all three GB models, suggesting that the dominant deformation mechanism *of* n-B_4C is GBs sliding. In the GB1 model, the atomic strain analysis suggests that a larger portion of predisintegrated icosahedra leads to more fractured icosahedra along GBs, resulting in larger plastic deformation region. This is consistent with our QM study on GBs in B_4C showing that the high energy GB model is more ductile than the low energy GB model [36].

(iii) The maximum shear stress is achieved before failure initiates. The maximum shear stress for GB1, GB2, and GB3 are 28.45 GPa at 0.5 shear strain, 29.07 GPa at 0.33 shear strain, and 29.25 GPa at 0.37 strain, respectively [Fig. 1(a)]. As the grain size is reduced, the fraction of GB atoms in n-B_4C increases, leading to the decreased maximum shear stress. This explains the observed reverse Hall-Petch relationship in n-B_4C.

(iv) Amorphization appears as the shear strain passes the critical shear strains which are 0.5 for GB1, 0.33 for GB2, and 0.37 for GB3. The amorphous bands form at these crossover regions where predistorted icosahedra exist since they fracture more easily under severe stress conditions. These amorphous bands are along the GBs, as shown in Figs. 1(d2) and 1(e2). Thus, the continuous shear leads to amorphous band formation in the GBs regions [2–3 nm in width, shown in Figs. 1(d2) and 1(e2)], which significantly relieves the shear stress.

(v) Cavitation and crack initiation start after amorphous band formation, as shown in Figs. 1(d3) and 1(e3). The cavitation initiates within the amorphous bands for GB1,

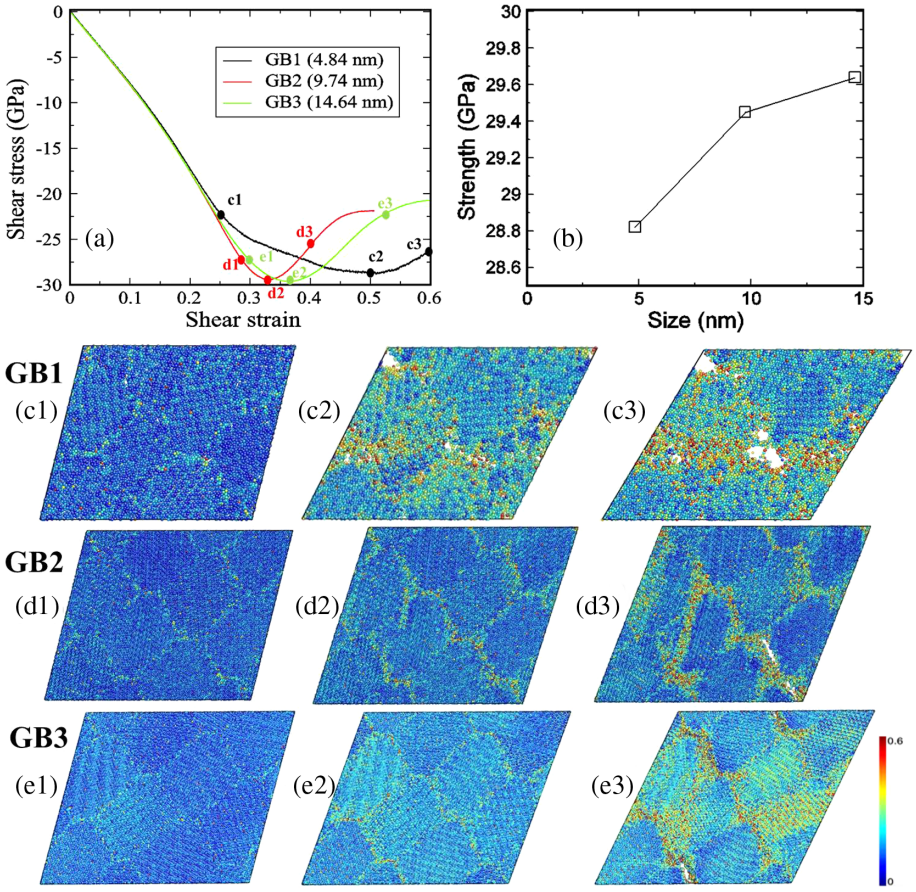

FIG. 1. (a) Stress-strain relationships of three GB models at finite shear deformation with shear rate of 0.1 ps^{-1}. (b) The shear strength of three GB models. (c1)–(e1) Snapshots of the beginning of plastic deformation for three GB models. (c2)–(e2) Snapshots of the end of plastic deformation, reaching the maximum shear strength. (c3)–(e3) Snapshots of the cavitation formation. Atoms are colored based on their atomic shear strain. The dimension of GB3 and GB2 are 3 and 2 times larger than GB1, respectively.

GB2, and GB3 at 0.45, 0.4, and 0.52 shear strain, respectively. Then, the crack opening further relaxes the shear stresses to 25.75 GPa for GB1, 21.50 GPa for GB2, and 20.40 for GB3. The crack opening in all three GB models suggests that the major facture mode in the *n*-B_4C is intergranular fracture. The experimental observation of transgranular fracture in microsized polycrystalline B_4C [37] may arise from microsize pores and secondary phases formed in the synthesis process.

Local deformation mechanism along GBs.—Previous experiments showed that GBs have a profound influence on mechanical properties of nanocrystalline ceramics, such as hardness, elastic modulus, and fracture behavior [10]. In order to extract the critical local state evolution of the GB under shear deformation, we analyze the shear stress and densities as a function of shear strain by selecting a 1 nm × 1 nm × 1 nm cube in one of the triple-junction regions of the GB2 model, as shown in Fig. 2. We extracted snapshots of the critical states to analyze the local deformation mechanism.

(i) First, the density keeps nearly constant as the shear strain increases to 0.2, indicating that this triple junction is undergoing an elastic deformation.

(ii) Both the shear stress and density increase slightly at 0.2 shear strain but start to decrease from 0.225 shear strain, suggesting deconstruction of some predistorted icosahedral clusters.

(iii) As the shear strain increases to 0.275, the shear stress reaches the maximum value of 32.23 GPa, which is higher than the maximum shear strength of the whole system [Fig. 1(b)]. This is due to the stress localization, leading to initiation of the amorphization.

(iv) Then, the continuous shear develops further amorphization, significantly relieving the shear stress to 11.96 GPa at 0.375 shear strain.

(v) Cavitation initiates in the amorphous region at 0.4 shear strain, which relaxes the shear stress to 0 while significantly decreasing the density to 0.12 g/m^3 at 0.475 shear strain because of the cavity formation.

Deformation response of n-B_4C through experimental measurements.—To validate these theoretical predictions on GB deformation and amorphization in *n*-B_4C, we performed nanoindentation tests on cantilever beams of the *n*-B_4C samples. The *n*-B_4C samples were prepared by high pressure sintering at a relatively low temperature of

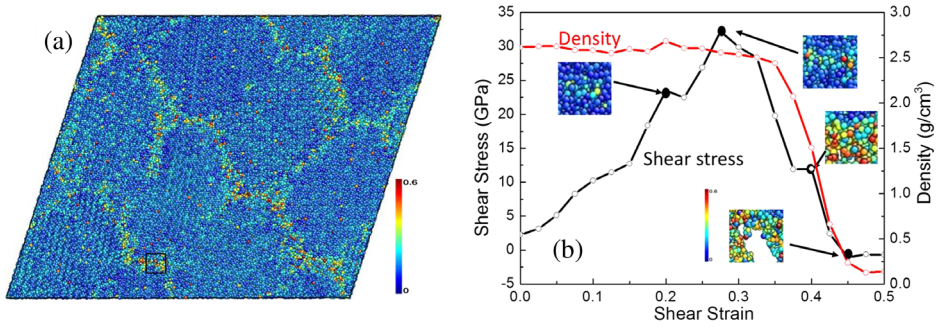

FIG. 2. (a) Snapshots of atomic configuration of GB2 at 0.325 shear strain. (b) Shear-stress−shear-strain and density-shear-strain relations of the 1 nm × 1 nm × 1 nm triple junction region [dark square in (a)]. Some snapshots of critical states are extracted. Atoms are color coded based on the atomic shear strain.

1600 °C using hot isostatic pressing in order to retain the original nanosize of B_4C green powders. A representative low magnification TEM image of the as-sintered n-B_4C shows mostly equiaxial grains with grain sizes ranging from 40 to 150 nm [Fig. 3(a)], which are the smallest grain size achieved in n-B_4C in the literature. Our TEM image shows clearly evidence for high densities of nanopores distributed homogenously throughout the sample, resulting from the lower sintering temperature. A high resolution TEM image acquired from a high-angle GB shows very sharp interface without detectable second phases [Fig. 3(b)]. In order to investigate and understand the deformation-failure mechanism of the n-B_4C, we carried out cantilever beam tests. Figure 3(c) shows a representative freestanding cantilever beam, imaged in a scanning electron microscope (SEM) image fabricated using a focused ion beam (FIB). We note that there are some pores on the surface in the cantilever near the pivot site, as indicated by black arrows in Fig. 3(c). These tests on cantilever beam specimens (L-49 μm, W-12 μm, and t-6.5 μm) were performed using nanoindentation by loading up to 5 mN within 1 s and keeping constant at 5 mN for 1000 s at very low strain rates of $\sim 10^{-8}$ 1/s. The indentation force was applied to the freestanding cantilever at the location shown by the red arrow [Fig. 3(c) and Fig. S2 of the Supplemental Material [30]]. The time displacement for tests at the red arrow position on n-B_4C sample is illustrated in Figs. S3 and S4 of the Supplemental Material [30]. The resultant time-displacement curve of cantilever deformation [Fig. 3(e)] shows a linear behavior initially, up to a displacement of ~255 nm, followed by deviation as estimated by slope of 0.01 1/nm, with a long time duration of about 1000 s. The small drops represented by black arrowheads in the displacement-time curve [Fig. 3(d)] may correspond to the sliding of individual fine grains, lying beneath the indenter. These observations suggest the presence of plastic deformation in n-B_4C, and we deduce that the experience of high stresses may cause grain sliding during nanoindentation. Figure 3(e) displays the SEM image of cantilever at the maximum loading force, in which fracture appears to have taken place in an intergranular mode at a large pore size on surface of the cantilever.

Local deformation characterization of n-B_4C.—To illustrate the precise underlying deformation of n-B_4C, we prepared a cross-sectioned thin foil from the indent region using FIB milling (Fig. S5 of the Supplemental Material [30]). We used TEM and scanning TEM (STEM)

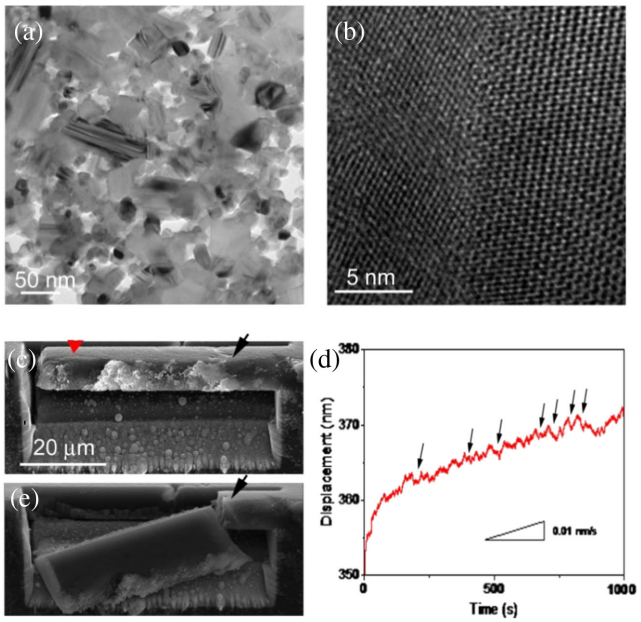

FIG. 3. Microstructural characterization and mechanical deformation of n-B_4C. (a) Low magnification TEM image of synthesized n-B_4C shows the fine-grain size ranges from 40 to 150 nm. (b) High resolution TEM image between two B_4C grains display the clean GB interface. (c) SEM image of a FIB prepared n-B_4C cantilever. Some nanopores are observed in the fabricated cantilever surface near the pivot surface. (d) Enlarged view of the loading segment with 5 mN constant load. Detectable permanent deformation is observed in n-B_4C and slope of 0.01 nm/s for reference. (e) SEM image of the cantilever after fracture at 6.145 mN loading force. The fracture took place at the pores in the cantilever.

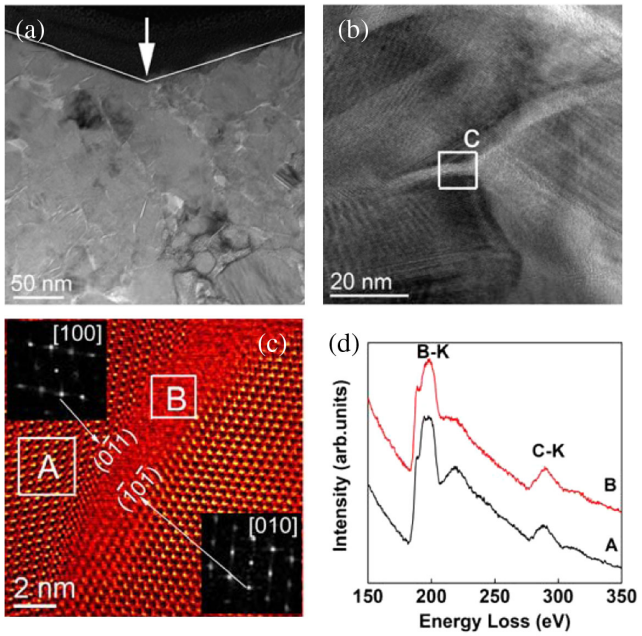

FIG. 4. TEM characterization of n-B_4C within the deformed region. (a) Low-magnification TEM of the deformed region beneath the indentation. No cracks are observed beneath the indenter surface. (b) High magnification TEM taken within the indentation displays amorphization at the triple junction GB interface. (c) ABF-STEM image obtained at the interface of two n-B_4C grains show clearly the amorphous band with a wide of about 2 nm. (d) EELS spectra obtained from the n-B_4C grain (A) and interface region (B) shows no difference in boron and carbon ratio suggesting that amorphization at the GBs has taken place during GB sliding that accompanies the significant plastic deformation before crack initiation.

observations to examine the underlying deformation mechanism of n-B_4C at the atomic level. The low magnification TEM image [Fig. 4(a)] beneath the indenter region shows clearly the elimination of nanoporosity as compared to as synthesized n-B_4C [Fig. 3(a)]. Furthermore, the high resolution TEM image [Fig. 4(b)] revealed a high degree of structural disorder (i.e., amorphous with a width of ~1.5 nm) at the triple junction point and GB. This suggests that the plastic deformation originates primarily from the GB amorphization which is most likely caused by GB sliding as suggested by the RMD simulations. Such an intergranular amorphous region could have formed to relieve the stress accumulation in the GB regions and triple junction points. Importantly, no dislocation activity or intragranular amorphous shear bands are observed, which is consistent with the theoretical prediction of the reverse Hall-Petch relation in nanocrystalline ceramics and B_4C. This behavior is different from microsized polycrystalline ceramics, such as alumina, silicon carbide, and boron carbide, which experience brittle failure by cleavage under high stresses [27,38,39]. Annular bright field STEM (ABF-STEM) [Fig. 4(c) and Fig. S5 of the Supplemental Material [30]] shows the atomic structure of the plastically deformed n-B_4C. The bright spots in the ABF-STEM image [Fig. 4(c)] represent a distinct atomic structure with a periodic arrangement of icosahedral clusters of B_4C. On the other hand, increased structure disorder with the formation of a visible amorphous zone can be observed at the GB, which is distinctly different from the crystalline structure [Fig. 4(c)]. The amorphous B_4C could be formed by GB shear deformation at the high contact pressure of nanoindentation. The STEM electron energy loss spectroscopy (EELS) spectra within the amorphous zone shows a boron (B) and carbon (C) ratio of 4:1 close to the n-B_4C grains [Fig. 4(d) and Fig. S6 of the Supplemental Material [30]]. These observations suggest that amorphous GBs contribute to the plastic deformation through GB sliding in the superhard n-B_4C.

GB sliding was observed directly in n-B_4C from RMD simulations. In addition, combining the nanoindentation and TEM experiments also suggested the GB sliding deformation mechanism in n-B_4C. It is worth noting that there are no nanopores in the simulation models while high densities of nanopores were present in the experimental samples because of relative low synthesizing temperature. Even the n-B_4C samples are different, the GB sliding are the dominate deformation mechanism in both porous n-B_4C and nonporous n-B_4C. Under highly compressive and shear stress nanoidentation conditions, these nanopores in n-B_4C are eliminated, which makes the experimental n-B_4C samples close to our models in RMD simulations. Practically, the observed intergranular amorphous GB phase under nanoindentation agrees very well with and validated by our RMD simulation prediction that the amorphous phase forms due to the GB sliding.

B_4C and related materials suffer from the brittle failure with very limited plastic deformation, which prevents their extended engineering applications. Therefore, it is essential to enhance their ductility and strength. Our current study on n-B_4C showed that GB sliding can significantly promote the plastic deformation and therefore enhance the ductility. In addition, the GB sliding facilitates the intergranular fracture rather than transgraunular fracture in microsize B_4C, enhancing the toughness. Therefore, a critical design to improve the ductility and toughness of B_4C is to decrease the grain size to nanoscale.

In summary, we examined the deformation mechanism of n-B_4C by combining microscale mechanical measurements, TEM observations, and ReaxFF RMD simulations. The deformation of n-B_4C displays a reverse Hall-Petch effect due to the GB sliding mechanisms. The ductility of n-B_4C increases as the grain size decrease to ~5 nm due to the high-energy GB development under shear deformation. The amorphous bands nucleate first at the intersections of GBs and then develop into 2–3 nm wide amorphous zones. These amorphous GB phases could have contributed to the significant plastic deformation to promote GB sliding in superhard B_4C ceramic. Our experimental and theoretical studies provide an atomic level explanation of the

deformation and failure of n-B_4C and reveal the intrinsic correlation between the reverse Hall-Petch relation and GB deformation and amorphization in the nanocrystalline ceramic.

This work is supported by National Science Foundation (CMMI-1727428). Q. A. was also supported by the U.S. Nuclear Regulatory Commission (NRC-HQ-84-15-G-0028). K. M. R. is supported by National Science Foundation China (Grant No. 51850410501) and seed funding from the School of Materials Science and Engineering at Shanghai Jiao Tong University (China). S. S. is supported by MOST 973 of China (Grant No. 2015CB856800). We would like to thank Professor Qiang Guo in the ShangHai JiaoTong University for use of the Fishone 1040 Nanomill system. We also thank Professor Shinoda at the Tokyo Institute of Technology (Japan) for providing as-synthesized n-B_4C samples for experimental observations. The authors declare no competing financial interests.

*D. G. and S. S. contributed equally to this work.
†Corresponding authors.
qia@unr.edu
kmreddy@sjtu.edu.cn

[1] E. O. Hall, Proc. Phys. Soc. London Sect. B **64**, 747 (1951).
[2] N. J. Petch, J. Iron Steel Inst. **174**, 25 (1953).
[3] I. A. Ovid'ko, Science **295**, 2386 (2002).
[4] J. A. Wollmershauser, B. N. Feigelson, E. P. Gorzkowski, C. T. Ellis, R. Goswami, S. B. Qadri, J. G. Tischler, F. J. Kub, and R. K. Everett, Acta Mater. **69**, 9 (2014).
[5] J. Schiøtz, F. D. Di Tolla, and K. W. Jacobsen, Nature (London) **391**, 561 (1998).
[6] M. A. Meyers, A. Mishra, and D. J. Benson, Prog. Mater. Sci. **51**, 427 (2006).
[7] Z. C. Cordero, B. E. Knight, and C. A. Schuh, Int. Mater. Rev. **61**, 495 (2016).
[8] H. Van Swygenhoven, Science **296**, 66 (2002).
[9] T. J. Rupert, D. S. Gianola, Y. Gan, and K. J. Hemker, Science **326**, 1686 (2009).
[10] H. Ryou, J. W. Drazin, K. J. Wahl, S. B. Qadri, E. P. Gorzkowski, B. N. Feigelson, and J. A. Wollmershauser, ACS Nano **12**, 3083 (2018).
[11] F. Liao, S. L. Girshick, W. M. Mook, W. W. Gerberich, and M. R. Zachariah, Appl. Phys. Lett. **86**, 171913 (2005).
[12] I. Szlufarska, A. Nakano, and P. Vashishta, Science **309**, 911 (2005).
[13] G. L. Messing and A. J. Stevenson, Science **322**, 383 (2008).
[14] I. W. Chen and X. H. Wang, Nature (London) **404**, 168 (2000).
[15] S. Vepřek, Z. Iqbal, and F. A. Sarott, Philos. Mag. B **45**, 137 (1982).
[16] N. K. Bourne, Proc. R. Soc. A **458**, 1999 (2002).
[17] A. O. Sezer and J. I. Brand, Mater. Sci. Eng. B **79**, 191 (2001).
[18] F. Thévenot, J. Eur. Ceram. Soc. **6**, 205 (1990).
[19] V. Domnich, S. Reynaud, R. A. Haber, and M. Chhowalla, J. Am. Ceram. Soc. **94**, 3605 (2011).
[20] F. Mauri, N. Vast, and C. J. Pickard, Phys. Rev. Lett. **87**, 085506 (2001).
[21] K. Y. Xie, Q. An, T. Sato, A. J. Breen, S. P. Ringer, W. A. Goddard III, J. M. Cairney, and K. J. Hemker, Proc. Natl. Acad. Sci. U.S.A. **113**, 12012 (2016).
[22] D. E. Grady, Mech. Mater. **29**, 181 (1998).
[23] D. Ghosh, G. Subhash, J. Q. Zheng, and V. Halls, J. Appl. Phys. **111**, 063523 (2012).
[24] T. J. Holmquist and G. R. Johnson, J. Appl. Phys. **100**, 093525 (2006).
[25] M. Chen, J. W. McCauley, and K. J. Hemker, Science **299**, 1563 (2003).
[26] T. Fujita, P. Guan, K. M. Reddy, A. Hirata, J. Guo, and M. Chen, Appl. Phys. Lett. **104**, 021907 (2014).
[27] K. M. Reddy, P. Liu, A. Hirata, T. Fujita, and M. W. Chen, Nat. Commun. **4**, 2483 (2013).
[28] Q. An, W. A. Goddard III, and T. Cheng, Phys. Rev. Lett. **113**, 095501 (2014).
[29] Q. An and W. A. Goddard III, Phys. Rev. Lett. **115**, 105501 (2015).
[30] See Supplemental Material at http://link.aps.org/supplemental/10.1103/PhysRevLett.121.145504, which includes Refs. [31–33], for (i) computational details, (ii) experiment details, (iii) Figs. S1 of simulation models of nanocrystalline B_4C, (iv) Figs. S2 of the schematic drawing of cantilever bending creep measurement, (v) Figs. S3 of displacement of the indenter, (vi) Figs. S4 of calculated creep strain, (vii) Figs. S5 of nanoindentation testing and TEM observations, (vi) Figs. S6 of STEM EELS of chemical mappings of amorphous interface.
[31] S. Plimpton, J. Comput. Phys. **117**, 1 (1995).
[32] I. Szlufarska, A. Nakano, and P. Vashishta, Science **309**, 911 (2005).
[33] K. M. Reddy, J. J. Guo, Y. Shinoda, T. Fujita, A. Hirata, J. P. Singh, J. W. McCauley, and M. W. Chen, Nat. Commun. **3**, 1052 (2012).
[34] J. Schiøtz and K. W. Jacobsen, Science **301**, 1357 (2003).
[35] F. Shimizu, S. Ogata, and J. Li, Mater. Trans., JIM **48**, 2923 (2007).
[36] X. Yang, S. P. Coleman, J. C. Lasalvia, W. A. Goddard III, and Q. An, ACS Appl. Mater. Interfaces **10**, 5072 (2018).
[37] K. Y. Xie, K. Kuwelkar, R. A. Haber, J. C. LaSalvia, K. J. Hemker, and R. Hay, J. Am. Ceram. Soc. **99**, 2834 (2016).
[38] K. M. Reddy, A. Hirata, P. Liu, T. Fujita, T. Goto, and M. W. Chen, Scr. Mater. **76**, 9 (2014).
[39] Q. An, K. M. Reddy, J. Qian, K. J. Hemker, M.-W. Chen, and W. A. Goddard III, Nat. Commun. **7**, 11001 (2016).